

# Shape Memory Polymers for Body Motion Energy Harvesting and Self-Powered Mechanosensing

Ruiyuan Liu, Xiao Kuang, Jianan Deng, Yi-Cheng Wang, Aurelia C. Wang, Wenbo Ding, Ying-Chih Lai, Jun Chen, Peihong Wang, Zhiqun Lin, H. Jerry Qi,\* Baoquan Sun,\* and Zhong Lin Wang\*

**Growing demand in portable electronics raises a requirement to electronic devices being stretchable, deformable, and durable, for which functional polymers are ideal choices of materials. Here, the first transformable smart energy harvester and self-powered mechanosensation sensor using shape memory polymers is demonstrated. The device is based on the mechanism of a flexible triboelectric nanogenerator using the thermally triggered shape transformation of organic materials for effectively harvesting mechanical energy. This work paves a new direction for functional polymers, especially in the field of mechanosensation for potential applications in areas such as soft robotics, biomedical devices, and wearable electronics.**

Functional polymers with exciting properties such as being flexible, foldable, stretchable, or shape-adaptive are promising for applications in soft robotics, biomechanics, and wearable/implantable electronics.<sup>[1–3]</sup> Triboelectric nanogenerators (TENGs) are usually made of organic materials for converting ambient mechanical energy into electric signals based on triboelectrification and electrostatic induction. TENGs have been demonstrated as effective energy harvester and self-powered sensors for pressure, motion, and chemical

and acoustic wave detection.<sup>[4–13]</sup> Several shape-adaptive and stretchable TENGs have been developed by using structural designs such as wavy Kapton film, kirigami paper, or elastic materials including polydimethylsiloxane (PDMS) and silicone rubber.<sup>[14–16]</sup>

Shape memory polymers (SMPs), a kind of stimulus-responsive material, are capable of maintaining a temporary shape and recovering their initial shape in the presence of an external stimulus, such as thermal or light.<sup>[17–23]</sup> For thermally triggered SMPs, a temporary shape could be fixed through deforming the

material above a transition temperature ( $T_t$ ) (either the melting temperature or the glass transition temperature) and cooling down. The material would then recover its permanent shape when the temperature is higher than  $T_t$  again in the absence of an external force owing to the entropic elasticity. This unique shape programmable property makes SMPs a promising candidate in various fields such as biomedical devices, soft robotics, flexible electronics, and aerospace applications.<sup>[24–30]</sup>

Here, we report an SMP-based TENG (STENG) to harvest biomechanical energy and detect biomechanical motion. Taking advantage of the special properties of SMPs and a conductive liquid electrode, the STENG is able to transform its shape according to different requirements and hold on to temporary configuration. In addition, the STENG can act as an energy harvester as well as a self-powered, wearable, biomechanical sensor. This work represents a new application of SMPs for energy harvesters, self-powered sensors, soft robotics, and actuators.


The SMP was synthesized by incorporating a semicrystalline thermoplastic polymer in a chemically cross-linked elastomer, forming a semiinterpenetrating polymer network (semi-IPN), where the semicrystalline thermoplastic polymer chains were immersed in the elastomer network.<sup>[31–33]</sup> As a demonstration here, a photocurable resin mixture containing acrylate and semicrystalline polycaprolactone (PCL) was cured in a mold under UV illumination, enabling a rapid and tailor-made design of initial shape. A series of samples containing different contents of PCL were prepared. The mechanism of shape memory behavior is shown in **Figure 1A**. When the SMP was deformed at a temperature above the melting temperature ( $T_m$ ) of PCL, the small crystals melt and deformed with the elastomer network. However, the melt in microphase regions

Dr. R. Liu, Dr. J. Deng, Dr. Y.-C. Wang, A. C. Wang, Dr. W. Ding, Prof. Y.-C. Lai, Dr. J. Chen, Prof. P. Wang, Prof. Z. Lin, Prof. Z. L. Wang  
School of Materials Science and Engineering  
Georgia Institute of Technology  
Atlanta, GA 30332, USA  
E-mail: zlwang@gatech.edu

Dr. R. Liu, Prof. B. Sun  
Institute of Functional Nano and Soft Materials  
Soochow University  
Suzhou, Jiangsu 215123, China  
E-mail: bqsun@suda.edu.cn

Dr. X. Kuang, Prof. H. J. Qi  
George W. Woodruff School of Mechanical Engineering  
Georgia Institute of Technology  
Atlanta, GA 30332, USA  
E-mail: qih@me.gatech.edu

Prof. Z. L. Wang  
Beijing Institute of Nanoenergy and Nanosystems  
Chinese Academy of Science  
National Center for Nanoscience and Technology  
Beijing 100083, China

 The ORCID identification number(s) for the author(s) of this article can be found under <https://doi.org/10.1002/adma.201705195>.

DOI: 10.1002/adma.201705195

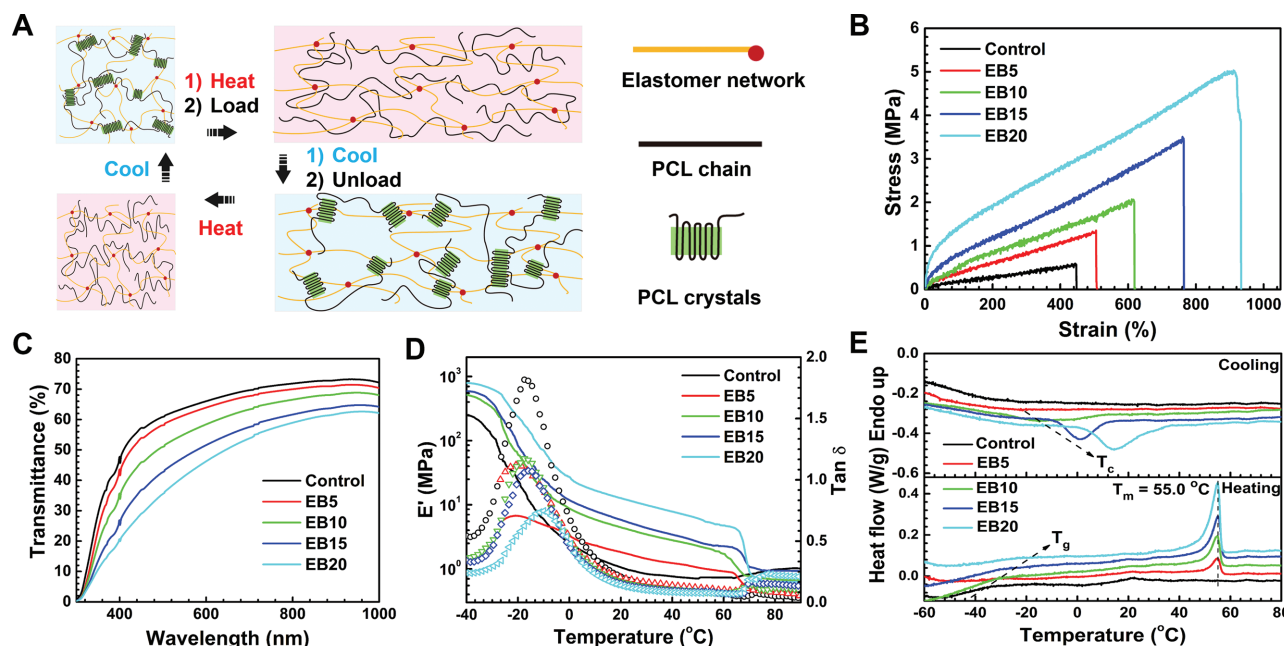


**Figure 1.** Property characterization of the SMP. A) Schematics showing the mechanism of shape memory behavior. B) Tensile stress–strain curves, C) transmission spectra with  $\approx 350\ \mu\text{m}$  in thickness, D) DMA heating curves, and E) DSC cooling (upper) and heating curves (lower) of the EB film samples.

still retained connectivity by the long PCL chain. Upon cooling down without releasing the load, the PCL chains reformed a physically cross-linked network via small crystals, which could lock the deformed network.<sup>[31]</sup>

The mechanical properties of the SMPs were investigated by tensile tests. As shown in Figure 1B and Table S1 (Supporting Information), all of the samples behaved as typical elastomers with large fracture strains. Interestingly, both the Young's modulus, fracture stress and fracture strain increased with the PCL content. When 20 wt% of PCL was added, SMP sample (EB20) showed fracture strain as high as 900%. This is attributed to reinforcing effect of small PCL crystals that can retard the propagation of microcracks in the elastomer at large stretching. Thus, the incorporation of PCL into the soft acrylate network could improve both the modulus and toughness of SMP. The transmittance of the SMPs sample was investigated as shown in Figure 1C. Within the spectrum range from 300 to 1000 nm, the transmittance of the SMP samples showed a monotonic increase in the visible region and became relatively flat in the near-infrared region. The transmittance of SMP samples decreased with PCL content due to enhanced degree of crystallinity. The film exhibited a transmittance of about 50% in the visible region with a film thickness of  $\approx 350\ \mu\text{m}$ , which could be further improved by decreasing the film thickness.

The dynamic mechanical analysis (DMA) was performed for the SMP material under program heating (Figure 1D). All of the samples showed two separated thermal transitions corresponding to the glass transition temperature ( $T_g$ ) of the elastomer and the  $T_m$  of the PCL, respectively. Since  $T_g$  was much lower than room temperature, the material was a typical elastomer with the room temperature modulus lower than 10 MPa. The first plateau modulus increased with the amount of PCL content. While PCL melting occurred at almost the same

temperature for all of the SMPs. Above the  $T_m$  of PCL, the SMP materials showed a rubbery plateau with a modulus of about 0.1–0.25 MPa. The thermal transitions of SMP were also studied using differential scanning calorimetry (DSC) thermograms as shown in Figure 1E. After incorporating different contents of PCL, the samples showed a thermal transition near  $-40\ ^\circ\text{C}$  and an obvious endothermal peak at  $55\ ^\circ\text{C}$  in the heating run due to the glass transition of elastomer and melting of PCL, respectively. PCL melting temperature changed little with the PCL content. A higher PCL content led to a larger amount of crystals, as indicated by the larger endothermal peak area. During cooling, PCL crystallization showed an exothermic peak below  $20\ ^\circ\text{C}$ , which shifted to low temperature with decreasing content of PCL. In the following text, the SMP sample containing 20 wt% of PCL (denoted as EB20) was mainly used.

The shape memory properties of the semi-IPN elastomer were qualitatively demonstrated by using films. The planar films was deformed into different shapes at the temperature above  $T_m$  and fixed by cooling down to room temperature. For example, a rectangular strip can change into spring shape as a temporary shape (Figure 2A). The as-transformed polymers still inherited the elastomer properties of the original sample (Movie S1, Supporting Information). Shape recoveries were then triggered by using a heat gun. As shown in Figure 2B, the surface temperature of the curve-shaped band was about  $29.7\ ^\circ\text{C}$ , catching by a forward looking infrared (FLIR) camera. After heating with a heat gun, the spring turned to planar structure with a captured surface temperature of about  $54.8\ ^\circ\text{C}$  (Figure 2B; Movie S2, Supporting Information). In addition, curve-shaped, folded as well as spark-like samples also recovered their original shape upon heating, which confirmed the shape memory properties of the polymers (Movies S3–S5, Supporting Information). Furthermore, it could be observed

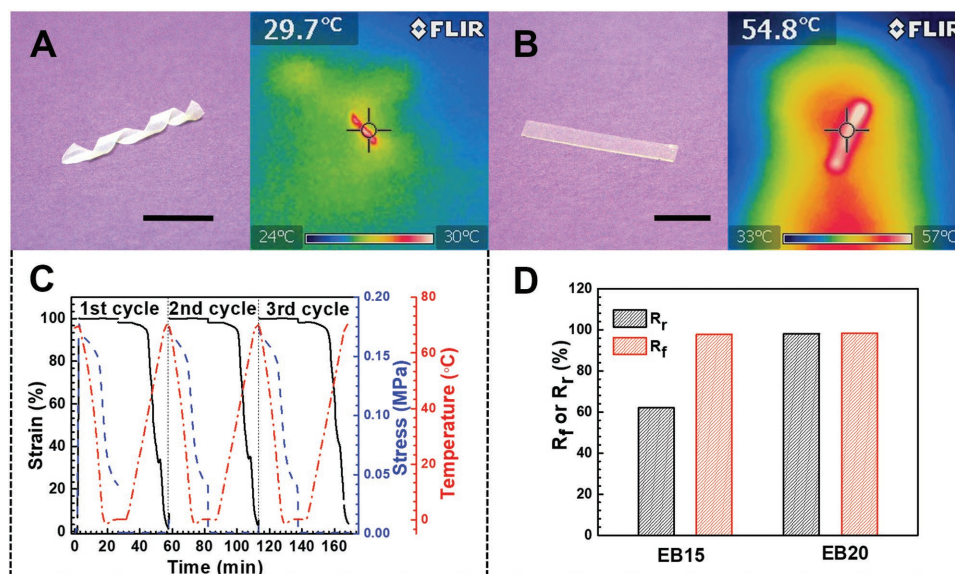


**Figure 2.** Shape memory behaviors of the SMP. A) EB20 sample with temporary spring shape and B) after reverting to the original shape along with the corresponding thermal images. The scale bars for all of the images are 2 cm. C) Shape memory cycle of the EB20 sample measured by DMA. D)  $R_f$  and  $R_r$  calculated for EB15 and EB20 samples.

that the opaque samples turned into transparent due to the melting of the crystallites upon raising temperature, which offers an alternative strategy to tune the optical property of the polymer.

The shape memory behavior of the SMPs was quantitatively characterized by DMA (Figure 2C). The shape fixing and recovery process was repeated for three cycles. The shape memory properties were quantitatively evaluated by the fixing ratios ( $R_f$ ), which quantify the ability to fix the temporary transient shape, and the recovery ratios ( $R_r$ ), which describe the capability of the SMP to restore the permanent shape. EB20 showed  $R_f$  and  $R_r$  over 97% for three cycles, indicating excellent shape fixity and shape recovery capability (Figure S1, Supporting Information). The content of PCL plays a key role on the shape memory properties. As shown in Figure 2D, the shape fixity increased with the PCL content and the shape recovery was comparable for EB15 and EB20. The SMP with the PCL content lower than 15 wt% was relatively weak at elevated temperature and showed poor shape memory properties. It is noted that the cooling rate would have some influences on crystallinity, especially the crystallization kinetics, but have little effect on the shape fixity. As the  $T_g$  of the polymer is very low (less than  $-10$  °C by DMA), the polymer chain has high mobility to crystallize upon cooling down. With the cooling rates of 5 and 10 °C min<sup>-1</sup>, comparable crystallinity can be obtained (Figure S2, Supporting Information). Basically, the shape fixity would be affected by the crystallinity. However, in the experimental shape memory test, the materials were cooling down under load and deformation was held at low temperature for a period of time. Consequently, comparable crystallinity and shape fixity can be obtained during the whole shape fixing process with different cooling rates.

To investigate the property of the nanogenerator, a device based on the single-electrode mode was first designed.<sup>[34]</sup> The STENG was fabricated as illustrated in Figure 3A, where

conductive liquid was sealed inside the SMP and a metal belt or a wire was used for electrical connection. Once an object with different electron affinity contacts with the polymer, electrification occurs at the interface and results in an equal amount of charges with opposite polarities between the two surfaces through electron injection. In the case electron affinity of the polymer is higher than the object, electrons will be injected into the surface of the polymer, thus it is more “negative” (Figure 3B). Upon the separation of the two surfaces, negative triboelectric charges will be remained on the surface of the SMP, and a layer of excessive positive ions will be formed in the conductive liquid due to the electrification induction effect. Electron will flow from the metal to the ground through external circuit to achieve potential equilibrium with the increase of the separation distance. When the positively charged object approaches the polymer, the induced positive charges in the conductive liquid decrease and the electrons flow from the ground back to the liquid until the two surfaces are fully contact with each other again, upon which the transferred charges will reach the maximum values. A full working cycle of process will generate alternating current while the electrons flow back and forth between the ground and the conductive liquid. Since amplitude and polarization of the induced open-circuit voltage ( $V_{oc}$ ) depends on the difference of the electron affinity, a positive voltage signal in this case will imply a more tribopositive object compared with the SMP and vice versa.  $V_{oc}$  values were recorded and summarized in Figures 3C,D by contacting the polymer with different materials of which the electron affinities have been studied using a linear motor (contact area, 2 cm × 2 cm; contact frequency, 1 Hz; contact force, 10 N; largest contact–separation distance ( $d$ ), 20 cm).<sup>[5]</sup> Compared with our SMP, paper, acrylic, and polyester (PET) were more tribopositive with a trend to lose electrons, while polydimethylsiloxane and silicone rubber were more tribonegative with a reversed  $V_{oc}$  signal. The  $V_{oc}$  also increased with



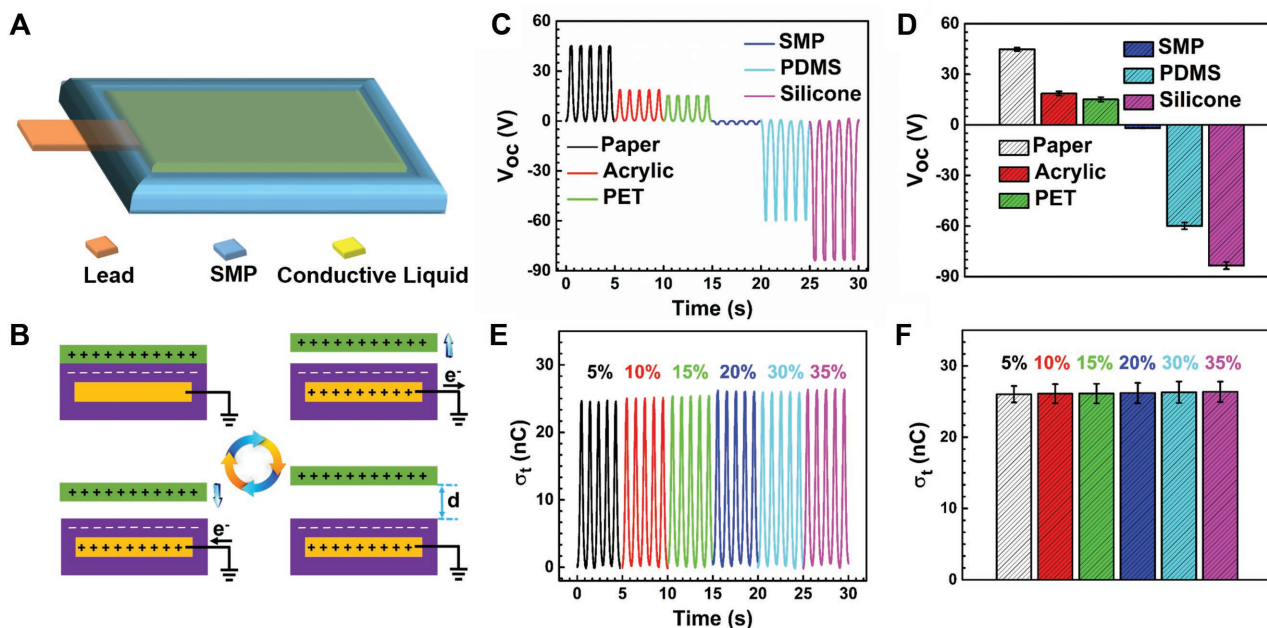


**Figure 3.** Design, operation mechanism, and structural optimization of the STENG. A) Schematic of the STENG. B) Schematic of the operation mechanism of the STENG in single-electrode mode. C)  $V_{oc}$  profiles and D) the summarized results of the STENG in contact with different materials. E) Output charge and F) the corresponding summarized values of the STENG with different NaCl weight concentrations.

the larger difference in the electron affinities, which was well consistent with the triboelectric series table.<sup>[5]</sup> The results showed that our SMP was moderate triboelectric material between PET and PDMS, and the highest  $V_{oc}$  was achieved when it contacted with silicone rubber, the most triboelectric material used in the test, as well as a superior deformable material for full contact. The concentration of the conductive liquid (NaCl solution was used here) was varied to investigate its effect on the output performance on the STENG. The measured transferred charges ( $\sigma_t$ ) were almost unchanged with increasing NaCl concentration from 5% to 35% (over saturated), which could be attributed to the high inherent impedance of the STENG ( $\approx M\Omega$ ) as observed before when compared with the resistance change of the liquid.<sup>[21]</sup> The nontoxic conductive liquid not only favors a deformable and stretchable device without an expensive process to fabricate flexible electrode, but also allows change of the appearance of the device. The STENG based on the nonopaque SMP could change the color by mixing inks with different colors into the liquid rather than the monotonous black rubber, which is more attractive considering the potential application in wearable devices (Figure S3, Supporting Information).

Typical output performance of the STENG including  $\sigma_t$ ,  $V_{oc}$  and short-circuit current density ( $J_{sc}$ ) were investigated by applying a 10 N force at different frequencies and  $d$  with a linear motor (NaCl solution, 35 wt%; contact area, 3 cm  $\times$  4 cm) working in a two-electrode contact-separation mode, as shown in Figure 4. The STENG exhibited a  $J_{sc}$  of  $\approx 1$  mA  $m^{-2}$ , a  $V_{oc}$  of  $\approx 220$  V, and a  $\sigma_t$  of  $\approx 73$  nC at a frequency of 1 Hz and a  $d$  of 20 cm. With the increase of the frequency,  $\sigma_t$  and  $V_{oc}$  almost remained unchanged, which was attributed to the constant contact area under this conditions.<sup>[34]</sup> The  $J_{sc}$  increased from  $\approx 1$  to  $\approx 3$  mA  $m^{-2}$  when the frequency increased from 1 to 4 Hz since the current flow is inversely proportional to time ( $T$ )

in the given charge ( $I_{sc} = d\sigma_t/dT$ ). By measuring the current density across the external load resistance connected in series, the output power density was calculated as  $IR^2/A$ , where  $I$  is the output current density,  $R$  is the load resistance, and  $A$  is the effective contact area (Figure 4D). A maximum power density of  $\approx 282$  mW  $m^{-2}$  was achieved at a matched resistance of 1000  $M\Omega$ . Both of the  $\sigma_t$  and  $V_{oc}$  increased with the rise of  $d$ , while  $J_{sc}$  also went up with the increasing  $d$  and frequency (Figures 4E,F), which were consistent with the previous result.<sup>[21]</sup>

The STENG could be used as a power source for electronics driven by human motion. The as-fabricated device was able to light up 150 green light-emitting diodes (LEDs) connected in series by hand tapping with a silicone rubber, demonstrating its superior ability as a mechanical energy harvester (Figure 5A; Movie S6, Supporting Information). A rectifier was used to regulate the output of the STENG by hand tapping using a silicone film to charge a 100  $\mu F$  capacitor (Figure 5B). The capacitor could drive an electronic watch (without battery; Movie S7, Supporting Information) when its voltage was charged to be over 1.5 V in 180 s, while the higher the voltage is, the longer the capacitor could power the watch. Being stretchable, deformable, and durable are important device requirements in the application of wearable electronics. The STENG could maintain its performance after being stretched by 60% while keeping the area of silicone constant (Figure 5C; Figure S4, Supporting Information), which meant that the whole output performance of the stretched device was improved if the enlarged area was counted. It is worth noting that by varying the amount of conductive liquid in the STENG, the stretchability of the device could be well tuned as the fracture strain of the materials was much higher than this value. All of the reported deformable devices should keep the external load to

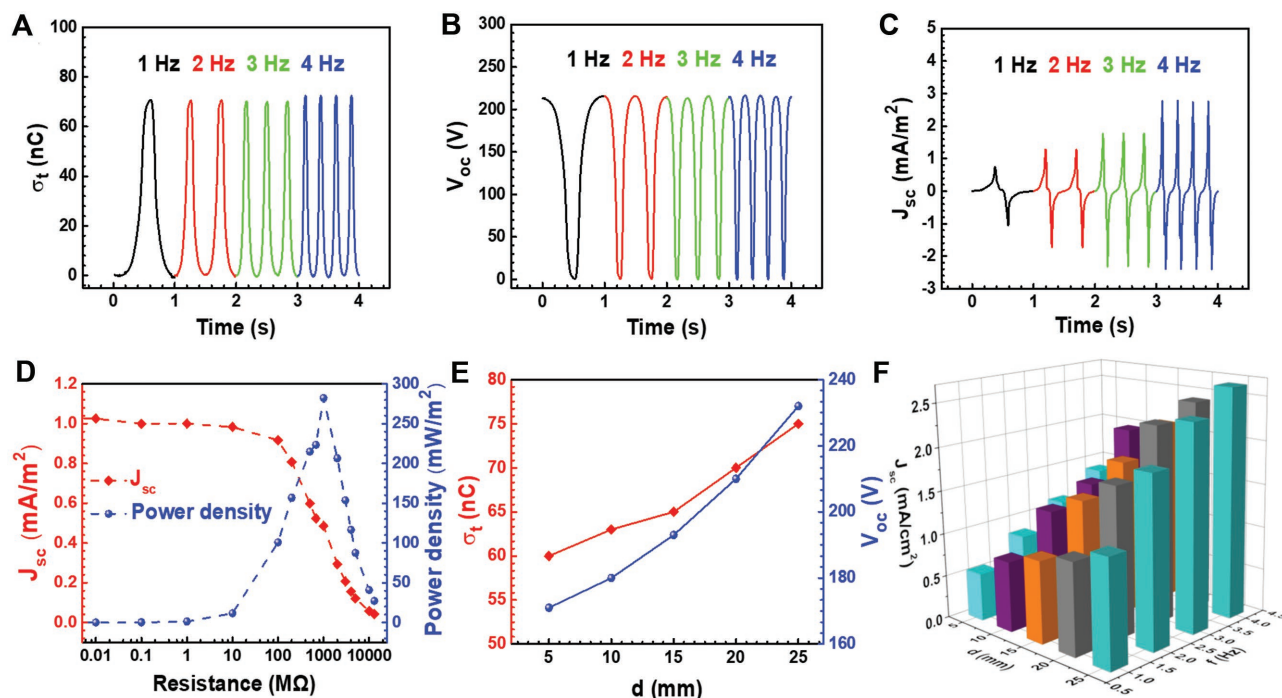


**Figure 4.** Output performance of the STENG in the contact–separation mode. A)  $\sigma_t$ , B)  $V_{oc}$ , and C)  $J_{sc}$  of the STENG. D) Relationship between the instantaneous output current density and power density with resistance of the external load. E) Dependence of the  $\sigma_t$  and  $V_{oc}$  on the largest distance between the two contact surfaces,  $d$ . F) Dependence of the  $J_{sc}$  on the contact–separation frequency and  $d$ .

hold their deformed shape, which was equivalent to make the device stretchable. In this case, the STENG was able to fix its deformed shape without any external force after the thermal process as mentioned above, making it a transformable TENG. Figures 5E,F show images of the STENG in its original shape

and after being stretched by over 50% with thermal treatment, respectively. As is clearly shown, the elongated device was well maintained after the thermal process. The device was able to recover its original shape after another thermal stimulation (Figure 5G) and change to a curve shape while adapted to

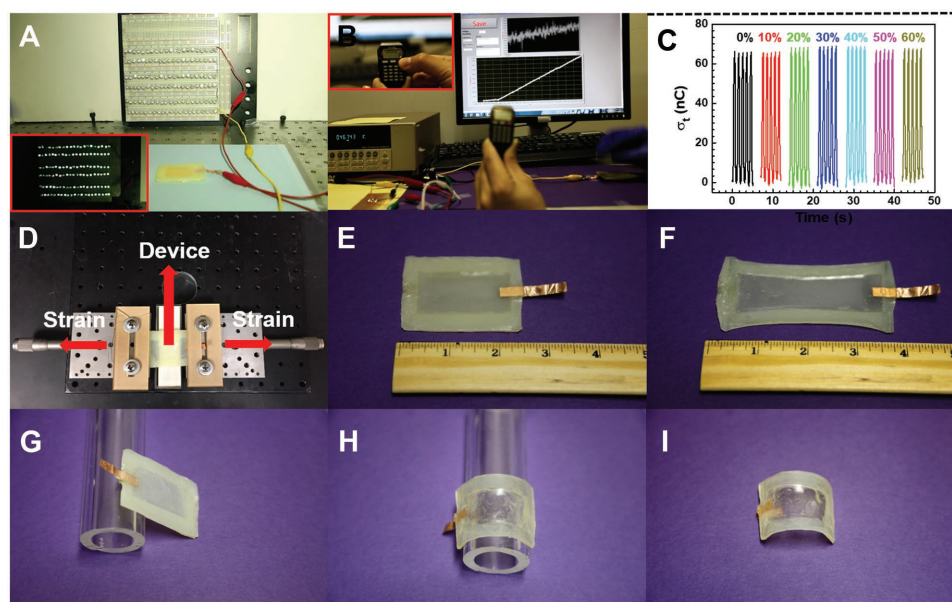


**Figure 5.** Stretchability and shape-memorized transformation ability of the STENG. A) Images of 150 green LEDs lit by the STENG when being tapped. B) Images of an electronic watch powered by tapping on the STENG. C)  $\sigma_t$  of the STENG under different strains. D) Image of the setup for strain test. Images of a STENG E) before and F) after being stretched by 50% and thermally processed. Images of a STENG G) before, H) during, and I) after being deformed on the surface of a tube.

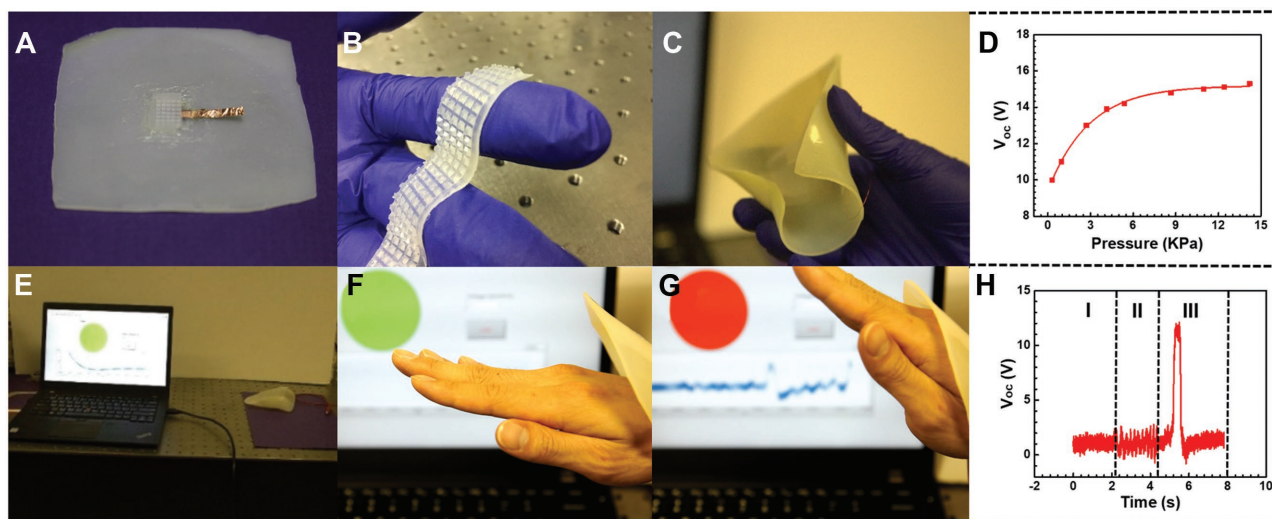


**Figure 6.** Demonstration of the STENG as a mechanosensation sensor in the form of a shape adaptive wrist splint. A) A film-like STENG before thermal shaping. B) An image of the pyramid structured silicone rubber. C) An image of the splint STENG after being transformed on a wrist. D) Relationship of the applied pressure and the induced  $V_{oc}$  of the STENG. E) Setup of the smart splint alert system. F) Working mode of the smart splint system in states I and/or II with a green logo. G) Working mode of the smart splint system in state III with a red alarm. H) The voltage signal from the splint induced by movements between hand and the STENG. There are three different corresponding motion states of hand: I, still; II, moving but not touching on the splint; III, touching on the splint.

a tube (Figures 5H,I). This unique property makes the STENG a smart design that could be applied to various areas, such as complicated soft robotics and implanted medical devices. To examine the durability of the STENG, a long-termed motion test was carried out. The STENG was able to remain 97% of its initial performance after  $\approx 21\,000$  cycles, proving the excellent durability of the dielectric materials (Figure S5, Supporting Information).

The output signal of the TENG induced from mechanical motion is touch sensitive and thus it could be used as a self-powered mechanical sensor.<sup>[35]</sup> Smart materials place the as-fabricated STENG beyond the conventional applications such as touch panel and flexible sensor. Carpal tunnel syndrome (CTS) is a medical condition arising from the compression of the median nerve, which is a possible result from the repetitive wrist work including computer work or work requires a strong grip.<sup>[36,37]</sup> As nowadays people are spending more time than ever on computer or cellphone, this syndrome is likely to occur among a larger group of people. It has been reported that  $\approx 5\%$  of people in the United States have CTS.<sup>[36,38]</sup> Wearing a wrist splint is an effective method to alleviate the symptoms. Here, we developed a STENG-based smart wrist splint with an alarm system that could be used to modify the wrist motion. A  $1.5\text{ cm} \times 1.5\text{ cm}$  sized TENG was fabricated on a large SMP film as shown in Figure 6A. To improve the sensitivity of the mechanosensation, a pyramid structured silicone rubber was encapsulated, which could induce larger contacting area change at a certain degree of pressure (Figure 6B). The film was then heated to over  $55\text{ }^{\circ}\text{C}$  and fitted on a wrist during the cooling process to achieve a desired shape (Figure 6C). It is worth noting that this process is repeatable to fit the splint on different wrist. The measured  $V_{oc}$  increased with the applied pressure, starting from 10 V at 0.2 kPa which was almost a very gentle touch, to  $\approx 15\text{ V}$  at 14.7 kPa (Figure 6D). To detect the motion of a wrist,

the signals were divided into three states by the motions: still, moving but not touching on the splint, and touching on the splint. A smart splint alert system was designed to analyze the collected data at real time and send out an alarm signal at certain motion (Figure 6E). As shown in Figure 6F, the logo was green when the wrist was still or moving slightly without touching the splint, which was defined as a normal motion range. While the output signal was above 10 V, indicating the back of the hand touching the splint, the green signal would turn to red to remind the holder (Figure 6G; Movie S8, Supporting Information). Figure 6H depicts the  $V_{oc}$  for the three different stages of motions, demonstrating the reliability of the smart alert system. The as-fabricated STENG-based splint could not only prevent repetitive extreme range of motion of the wrist through the feedback system, but also act as a behavioral modification during daily life. The self-powered feature of STENG-based mechanosensation could make this feedback system incredibly simple, without any external energy support if LEDs were properly used as the alarm. The shape memory property of this STENG also allows a reusable process to fit on another wrist, which makes the device user friendly for medical devices. While it is just an initial prototype, the STENG-based smart splint shows several potential advantages over the commercialized neurosplint considering the simple fabrication process and broad feasibility.

In summary, a stretchable, deformable, and transformable energy harvester as well as a self-powered mechanosensation sensor has been demonstrated with unique programmable features as triggered by thermal stimulation. The STENG is flexible, stretchable, and skin-compatible. The shape memory property makes it outstanding from all of the other deformable TENGs as the STENG could adapt to almost any surface configurations through a thermal process and preserve the shape without any external holding. In combination with



conductive liquid, the STENG is able to change its color as well as the shape, which could significantly broaden its application range. The pressure-responsive electrical output in certain range allows the STENG to be a mechanosensation sensor. A self-powered feedback splint has been developed by a simple process to detect the motion of a twist to alleviate CTS, which demonstrates its potential application in wearable medical devices. This work paves a new prospect for multifunctional power source and self-powered sensors based on responsive smart materials. Future research should focus on improving the output performance of the energy harvester through surface treatment to maximize the charge density, structure optimization, and power management to collect more energy. Multifunctional devices' design based on other novel polymer materials that have unique properties, such as light responsive and self-healing, should cast broad applications in soft robotics, medical devices, and artificial skins by an integration with energy storage devices to achieve sustainable power supply and precise data analysis/software design to develop sensitive self-powered mechanosensation sensors.<sup>[39–41]</sup>

## Experimental Section

**Materials Preparation:** The shape memory polymer resin was prepared by mixing a certain content of polycaprolactone ( $M_n = 70\,000 \approx 90\,000$ , Sigma-Aldrich) from 0 to 20 wt% (weight to the mass of photocurable resin) at 50 to 70 °C. The photocurable resin is made of Ebecryl 8413 (AUD, Ebecryl 8413, Allnex) and *n*-butyl acrylate (Sigma-Aldrich) with Ebecryl 8413/BA mass ratios of 1/1.5. Then, 1.5 wt% of Irgacure 819 [phenylbis (2,4,6-trimethylbenzoyl) phosphine oxide; Sigma-Aldrich] to the total mass was added as the photoinitiator. Finally, the photocurable resin was sandwiched between glass plates with spacer and cured by Salon Edge 36 W Professional UV Lamp for about 10 min. Flexible film samples were obtained by peeling off from the glass, which were denoted as EB<sub>x</sub> ( $x$  is the ratio of PCL). The sample without PCL is used as a control sample (denoted as Control).

**Materials Characterization:** Uniaxial tension test was performed on an MTS Universal Materials Testing Machine (Criterion Model 41) at room temperature. The samples with the dimension of about 20 mm × 4 mm × 0.3 mm were cut from a film. The stretch rate was 50 mm min<sup>−1</sup> with the gauge length of about 10 mm. At least three specimens were tested to obtain average values. DMA was conducted on a Q800 (TA instrument) tester with a tensile clamp in a “multifrequency-strain” mode with a frequency of 1 Hz and an amplitude of 20 μm. The test was performed using the heating rate of 3 °C min<sup>−1</sup> from −40 to 90 °C under a nitrogen atmosphere. DSC analysis was carried out on a Q200 (TA instrument) instrument using aluminum pans under nitrogen purge. The heating and cooling rate was 5 °C min<sup>−1</sup>. The optical transmittance spectra were measured by a Jasco V-630 spectrophotometer. The surface temperature was measured by FLIR i5.

**Shape Memory Test:** All of the quantitative shape memory tests were carried out using a DMA Q800 in a tensile mode under a “strain rate” mode. Briefly, a rectangular specimen was uniaxially deformed at 70 °C (above PCL  $T_m$ ) by ramping to 100.00% strain at 100% min<sup>−1</sup>. The sample was then cooled to 0 °C at 5 °C min<sup>−1</sup> while holding the external force constant followed by an isothermal hold for 10 min, and then unloading the force back to 0.001 N (a small preload) to finish the shape fixing process. Shape recovery of the fixed deformations was triggered by heating the sample to 70 °C at 3 °C min<sup>−1</sup>. Shape fixity ( $R_f$ ) and shape recovery ( $R_r$ ) values were calculated from the following two equations, respectively

$$R_f(x) = \frac{\varepsilon}{\varepsilon_{\text{load}}} \times 100\% \quad (1)$$

$$R_r = \frac{\varepsilon - \varepsilon_{\text{rec}}}{\varepsilon} \times 100\% \quad (2)$$

where  $\varepsilon_{\text{load}}$ ,  $\varepsilon$ , and  $\varepsilon_{\text{rec}}$  represent the strain before unloading, the strain after unloading, and the strain after recovery for a shape, respectively.  $\varepsilon_{\text{rec}}$  and  $\varepsilon$  were determined from the end of the strain plateau in the recovery curve.

**Device Fabrication and Measurement:** A film with a rectangular groove was made by UV curing the resin between a terrace die and a glass slide. A copper wire or a band was used as the electrode and another layer of elastomer film (≈600 μm) with the same area was covered onto the previous one and sealed by photocuring the resin as a glue. Then different concentrations of conductive liquid (NaCl solution here) were injected into the cavity by a syringe and further sealed. A linear motor (LinMot E1100) was used to provide the input of mechanical motions. The force applied by the motor was detected by a LabQuest Mini force gauge (Vernier). The electrical output parameters of the STENGs were collected by a programmable electrometer (Keithley, 6514) and recorded by a software written in LabVIEW.

## Supporting Information

Supporting Information is available from the Wiley Online Library or from the author.

## Acknowledgements

R.L., X.K., and J.D. contributed equally to this work. R.L., J.D., and X.K. conceived the idea, designed the experiment, and performed the measurement. W.D. designed the software. Z.L.W. guided the project. All authors discussed the results and commented on the manuscript. This research was supported by the Hightower Chair Foundation, and the “Thousands Talents” program for pioneer researcher and his innovation team. R.L. and J.D. would like to thank the support from the China Scholarship Council. X.K. and H.-J.Q. thank the support from HP Inc.

## Conflict of Interest

The authors declare no conflict of interest.

## Keywords

energy harvesting, self-powered mechanosensation, shape memory polymers, triboelectric nanogenerators

Received: September 10, 2017

Revised: October 29, 2017

Published online:

- [1] M. Kaltenbrunner, T. Sekitani, J. Reeder, T. Yokota, K. Kuribara, T. Tokuhara, M. Drack, R. Schwödiauer, I. Graz, S. Bauer-Gogonea, *Nature* **2013**, 499, 458.
- [2] D. Rus, M. T. Tolley, *Nature* **2015**, 521, 467.
- [3] D. Yang, B. Mosadegh, A. Ainla, B. Lee, F. Khashai, Z. Suo, K. Bertoldi, G. M. Whitesides, *Adv. Mater.* **2015**, 27, 6323.
- [4] F. R. Fan, Z. Q. Tian, Z. L. Wang, *Nano Energy* **2012**, 1, 328.

- [5] Z. L. Wang, *ACS Nano* **2013**, 7, 9533.
- [6] Z. L. Wang, J. Chen, L. Lin, *Energy Environ. Sci.* **2015**, 8, 2250.
- [7] G. Zhu, J. Chen, T. Zhang, Q. Jing, Z. L. Wang, *Nat. Commun.* **2014**, 5, 3426.
- [8] Y. Zi, S. Niu, J. Wang, Z. Wen, W. Tang, Z. L. Wang, *Nat. Commun.* **2015**, 6, 8376.
- [9] J. Chen, Y. Huang, N. Zhang, H. Zou, R. Liu, C. Tao, X. Fan, Z. L. Wang, *Nat. Energy* **2016**, 1, 16138.
- [10] C. Wu, R. Liu, J. Wang, Y. Zi, L. Lin, Z. L. Wang, *Nano Energy* **2017**, 32, 287.
- [11] K. Y. Lee, M. K. Gupta, S.-W. Kim, *Nano Energy* **2015**, 14, 139.
- [12] L. B. Huang, G. Bai, M. C. Wong, Z. Yang, W. Xu, J. Hao, *Adv. Mater.* **2016**, 28, 2744.
- [13] J. W. Lee, H. J. Cho, J. Chun, K. N. Kim, S. Kim, C. W. Ahn, I. W. Kim, J.-Y. Kim, S.-W. Kim, C. Yang, J. M. Baik, *Sci. Adv.* **2017**, 3, e1602902.
- [14] Y. C. Lai, J. Deng, S. Niu, W. Peng, C. Wu, R. Liu, Z. Wen, Z. L. Wang, *Adv. Mater.* **2016**, 28, 10024.
- [15] J. Wang, S. Li, F. Yi, Y. Zi, J. Lin, X. Wang, Y. Xu, Z. L. Wang, *Nat. Commun.* **2016**, 7, 43421.
- [16] F. Yi, X. Wang, S. Niu, S. Li, Y. Yin, K. Dai, G. Zhang, L. Lin, Z. Wen, H. Guo, *Sci. Adv.* **2016**, 2, e1501624.
- [17] T. Xie, *Nature* **2010**, 464, 267.
- [18] M. Zarek, M. Layani, I. Cooperstein, E. Sachyani, D. Cohn, S. Magdassi, *Adv. Mater.* **2016**, 28, 4449.
- [19] K. Yu, Q. Ge, H. J. Qi, *Nat. Commun.* **2014**, 5, 3066.
- [20] L. Huang, R. Jiang, J. Wu, J. Song, H. Bai, B. Li, Q. Zhao, T. Xie, *Adv. Mater.* **2017**, 29, 1605390.
- [21] Q. Zhao, W. Zou, Y. Luo, T. Xie, *Sci. Adv.* **2016**, 2, e1501297.
- [22] X. Luo, P. T. Mather, *ACS Macro Lett.* **2013**, 2, 152.
- [23] X. Kuang, G. Liu, X. Dong, D. Wang, *Polymer* **2016**, 84, 1.
- [24] Y. Liu, H. Du, L. Liu, J. Leng, *Smart Mater. Struct.* **2014**, 23, 023001.
- [25] J. G. Hardy, M. Palma, S. J. Wind, M. J. Biggs, *Adv. Mater.* **2016**, 28, 5717.
- [26] P. T. Mather, X. Luo, I. A. Rousseau, *Ann. Rev. Mater. Res.* **2009**, 39, 445.
- [27] Z. Ning, Y. Huang, Z. Qian, F. Xue, X. Tao, *Sci. Sin-Phys. Mech. Astron.* **2016**, 46, 44602.
- [28] T. Xie, X. Xiao, *Chem. Mater.* **2008**, 20, 2866.
- [29] W. Voit, T. Ware, R. R. Dasari, P. Smith, L. Danz, D. Simon, S. Barlow, S. R. Marder, K. Gall, *Adv. Funct. Mater.* **2010**, 20, 162.
- [30] H. Xu, C. Yu, S. Wang, V. Malyarchuk, T. Xie, J. A. Rogers, *Adv. Funct. Mater.* **2013**, 23, 3299.
- [31] X. Luo, P. T. Mather, *Macromolecules* **2009**, 42, 7251.
- [32] E. D. Rodriguez, X. Luo, P. T. Mather, *ACS Appl. Mater. Interfaces* **2011**, 3, 152.
- [33] Q. Ge, X. Luo, E. D. Rodriguez, X. Zhang, P. T. Mather, M. L. Dunn, H. J. Qi, *J. Mech. Phys. Solids* **2012**, 60, 67.
- [34] S. Niu, S. Wang, L. Lin, Y. Liu, Y. S. Zhou, Y. Hu, Z. L. Wang, *Energy Environ. Sci.* **2013**, 6, 3576.
- [35] X. Wang, H. Zhang, L. Dong, X. Han, W. Du, J. Zhai, C. Pan, Z. L. Wang, *Adv. Mater.* **2016**, 28, 2896.
- [36] C. Burton, L. S. Chesterton, G. Davenport, *Br. J. Gen. Pract.* **2014**, 64, 262.
- [37] J. N. Katz, B. P. Simmons, *N. Engl. J. Med.* **2002**, 346, 1807.
- [38] K. D. Bickel, *J. Hand Surg.* **2010**, 35, 147.
- [39] W. Xu, L.-B. Huang, M.-C. Wong, L. Chen, G. Bai, J. Hao, *Adv. Energy Mater.* **2017**, 7, 1601529.
- [40] L.-b. Huang, W. Xu, G. Bai, M.-C. Wong, Z. Yang, J. Hao, *Nano Energy* **2016**, 30, 36.
- [41] W. Xu, L.-B. Huang, J. Hao, *Nano Energy* **2017**, 40, 399.